

## Characterization of Ordered Mesoporous Silica Films Using Small-Angle Neutron Scattering and X-ray Porosimetry

Bryan D. Vogt,<sup>\*,†</sup> Rajaram A. Pai,<sup>‡</sup> Hae-Jeong Lee,<sup>†</sup> Ronald C. Hedden,<sup>†,§</sup>  
Christopher L. Soles,<sup>†</sup> Wen-li Wu,<sup>†</sup> Eric K. Lin,<sup>†</sup> Barry J. Bauer,<sup>†</sup> and James J. Watkins<sup>\*,‡</sup>

Polymers Division, National Institute of Standards and Technology, Gaithersburg, Maryland 20899-8541,  
and Department of Chemical Engineering, University of Massachusetts, Amherst, Massachusetts 01003

Received August 13, 2004. Revised Manuscript Received December 20, 2004

Ordered mesoporous silica films were synthesized using pre-organized block copolymer templates in supercritical carbon dioxide. Poly(ethylene oxide-*block*-propylene oxide-*block*-ethylene oxide), PEO-*b*-PPO-*b*-PEO, films doped with *p*-toluenesulfonic acid (*p*-TSA) were infused with carbon dioxide solutions of silica precursors. Silica condensation proceeded selectively in the hydrophilic PEO domain due to selective partitioning of the acid catalyst in the template during its preparation. Removal of the organic template by calcination at 400 °C yielded robust mesoporous films. The films were characterized using X-ray diffraction (XRD), spectroscopic ellipsometry (SE), X-ray reflectivity (XR), Rutherford backscattering (RBS), forward recoil elastic spectroscopy (FRES), transmission electron microscopy (TEM), and small-angle neutron scattering (SANS). The pore structure and distribution was probed using contrast variation SANS porosimetry and X-ray porosimetry. Two distinct populations of pores are present in the films. Spherical mesopores were templated by the hydrophobic domain of the copolymer. Micropores in the pore walls are present due to removal of the hydrophilic PEO block, which forms an interpenetrating network (IPN)-like structure with the silicate network during infusion and condensation of the precursor. The wall density was determined to be  $(1.95 \pm 0.05) \text{ g cm}^{-3}$  and the overall porosity was found to be 39 vol %, with good agreement between the SANS and X-ray reflectivity results. A significant fraction of the total porosity, 44% to 53%, in these materials is attributed to the micropores in the wall structure.

### Introduction

Since the discovery of synthetic routes to mesoporous silicates (MCM-41) in the early 1990s,<sup>1</sup> research on new mesoporous materials has thrived based on their potential in applications ranging from catalysis to separations to low dielectric constant (*k*) materials.<sup>2</sup> The typical synthesis route involves the cooperative assembly of silica precursors (or other metal oxide precursors) and surfactants, including nonionic amphiphilic block copolymers (BCPs) from aqueous alcohol solutions.<sup>3–5</sup> Pore dimension and morphology can be controlled through variation of the copolymer molecular mass, copolymer composition, solution concentration, and solution conditions (temperature and pH).<sup>3,6–8</sup> Films can be

produced by dip coating<sup>3</sup> or spin coating<sup>9</sup> via evaporation-induced self-assembly.<sup>10</sup> While cooperative assembly is a remarkably versatile approach, there are a number of limiting factors. Simultaneous structural evolution via cooperative assembly and precursor condensation to yield the silica network impose an inherent impediment to achieving long-range order and pore orientation, which are crucial for a number of applications. Precursor and template selection are predicated by the requirements of mutual solubility and cooperative assembly via specific interactions. Finally, the use of excess alcohol to moderate precursor condensation during assembly necessitates long aging periods.

Recently, we reported an alternative strategy for the synthesis of mesoporous materials that circumvents these issues.<sup>11</sup> The process involves the infusion and selective condensation of metal oxide precursors within one phase domain of a highly ordered, preformed block copolymer template diluted with supercritical carbon dioxide (Figure 1). The ordered template is prepared by spin coating an amphiphilic block copolymer onto a silicon wafer from solution containing an organic acid, which selectively partitions into the hydrophilic domain of the copolymer during solvent evaporation and self-assembly. The template

\* Corresponding authors. E-mail: bryan.vogt@nist.gov and watkins@ecs.umass.edu.

<sup>†</sup> National Institute of Standards and Technology.

<sup>‡</sup> University of Massachusetts.

<sup>§</sup> Present address: Department of Materials Science and Engineering, The Pennsylvania State University, University Park, PA.

(1) Kresge, C. T.; Leonowicz, M. E.; Roth, W. J.; Vartuli, J. C.; Bach, J. S. *Nature* **1992**, *331*, 698–699.

(2) Davis, M. E. *Nature* **2002**, *417*, 813–821.

(3) Yang, P.; Zhao, D.; Margolese, D. I.; Chmelka, B. F.; Stucky, G. D. *Nature* **1998**, *152*.

(4) Forster, S.; Antonietti, M. *Adv. Mater.* **1998**, *10*, 195–217.

(5) Zhao, D.; Feng, J.; Huo, Q.; Melosh, N.; Fredrickson, G. H.; Chmelka, B. F.; Stucky, G. D. *Science* **1998**, *279*, 548–552.

(6) Galarneau, A.; Cambon, H.; Di Reszno, F.; Fajula, F. *Langmuir* **2001**, *17*, 8328–8335.

(7) Imperor-Clerc, M.; Davidson, P.; Davidson, A. *J. Am. Chem. Soc.* **2000**, *122*, 11925–11933.

(8) Kruk, M.; Jaroniec, M.; Ko, C. H.; Ryoo, R. *Chem. Mater.* **2000**, *12*, 1961–1968.

(9) Balkenende, A. R.; de Theije, F. K.; Kriege, J. C. K. *Adv. Mater.* **2003**, *15*, 139–143.

(10) Brinker, C. J.; Lu, Y.; Sellinger, A.; Fan, H. *Adv. Mater.* **1999**, *11*, 579–585.

(11) Pai, R. A.; Humayan, R.; Schulber, M. T.; Sengupta, A.; Sun, J.-H.; Watkins, J. J. *Science* **2004**, *303*, 507–510.

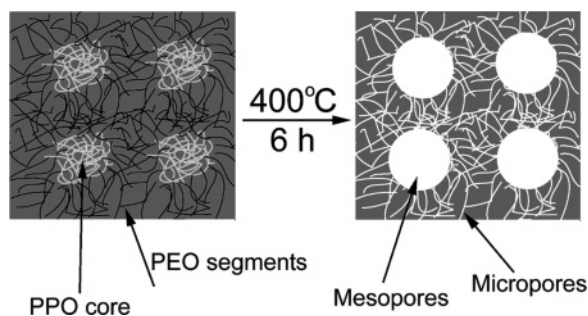


**Figure 1.** Mesopores and micropores in a block copolymer templated silicate film.

is then annealed and exposed to a solution of silicon alkoxide(s) in humidified supercritical carbon dioxide. Modest dilation of the polymer film by CO<sub>2</sub> sorption facilitates rapid diffusion of the reagents<sup>12</sup> and the precursor condenses within the acidic hydrophilic domain of the template to form the metal oxide network. No reaction occurs in the fluid phase or in the hydrophobic domain due to localization of the catalyst. Finally, the template is removed to produce the mesoporous oxide. To date, we have replicated ordered spherical and cylindrical template morphologies to yield silica, organosilicate, and mixed silica/organosilicate mesostructures in films greater than 1  $\mu\text{m}$  thick, while maintaining structural details of the sacrificial copolymer template. Because template formation and silicate network condensation occur in discrete steps, film structure and matrix composition can be independently controlled by template manipulation prior to infusion and selection of appropriate precursors. Thus, prescriptive control of porous films is now possible. Moreover, the elimination of excess alcohol from the reaction media provides a pathway for rapid and high degrees of network condensation and thus minimal shrinkage during template removal. Conceptually, the two-step template formation and supercritical fluid (SCF) infusion approach yields materials that are structurally distinct from those prepared by cooperative self-assembly using identical precursors and surfactants. In the SCF approach, the silicate network is prepared by condensation within a dilated template polymer, yielding an IPN-like structure in the pore wall prior to template removal (see Figure 1). Microporosity in the pore wall arising from template removal should depend on silicate network loading within the hydrophilic domain of the copolymer and can be controlled.<sup>11</sup> One objective of this paper is to determine if these structural differences are present.

While numerous routes for the preparation of mesoporous metal oxides have been developed, complete characterization of these materials, including pore size, distribution, and connectivity remains a challenge. Typical characterization techniques for mesoporous materials include X-ray diffraction (XRD), transmission electron microscopy (TEM), thermogravimetric analysis (TGA), and N<sub>2</sub> adsorption.<sup>3,5–8</sup> Positron annihilation spectroscopy (PAS/PALS) has been used to probe pore shape and pore size distribution,<sup>13,14</sup> but

the results are model-dependent and can be difficult to interpret when there is a high degree of pore connectivity.<sup>15</sup> Nuclear magnetic resonance (NMR) spectroscopy has also been used to characterize the pore size distribution.<sup>16</sup> Despite recent progress, accurate determination of pore size distribution (PSD) remains a challenge. Calculation of PSD from N<sub>2</sub> adsorption data requires an accurate model for capillary condensation.<sup>17</sup> Unfortunately, the Kelvin equation or simple modifications thereof often give inaccurate values for the pore sizes,<sup>18</sup> although quantitative agreement from N<sub>2</sub> adsorption experiments with XRD data has been found in some cases.<sup>19,20</sup> However, the exact mechanism for the adsorption cannot be confirmed by N<sub>2</sub> adsorption alone. By coupling the N<sub>2</sub> adsorption measurement with small-angle neutron scattering (SANS), the structure of the mesoporous material can be elicited during the adsorption process<sup>21</sup> as it is possible to distinguish the pore-filling mechanism. With use of this approach, micropores arising from removal of the hydrophilic block of mesoporous silica prepared by cooperative self-assembly were observed directly. Their presence was previously inferred from XRD,<sup>7</sup> high-resolution TEM,<sup>22</sup> and N<sub>2</sub> adsorption<sup>6,8</sup> experiments. However, SANS measurements were performed at relatively few relative pressures, limiting the characterization of the pore-filling process.<sup>21</sup> The N<sub>2</sub> adsorption/SANS combination also has the limitation that the neutron scattering length density (NSLD) of the wall material must be fortuitously matched by the NSLD for the adsorbed nitrogen for tractable analysis, significantly limiting the materials that can be characterized using this approach. Recently, SANS contrast variation was used to characterize the PSD of low-*k* dielectrics.<sup>23</sup> In this case, toluene vapor was used instead of N<sub>2</sub> as the pore-filling agent, as the NSLD for organic compounds can be controlled by selective deuteration. By using mixtures of protonated (h) and deuterated (d) toluene, the NSLD of the solvent can be tuned to match the NSLD of the pore walls.<sup>24</sup>

There are numerous approaches to determine the total porosity of mesoporous materials. The porosity of thin films can be obtained from ellipsometric porosimetry (EP), X-ray porosimetry (XRP), PAS/PALS, surface acoustic wave spectroscopy (SAWS), and traditional N<sub>2</sub> adsorption with reasonable agreement between the techniques.<sup>25,26</sup> EP and XRP require a probe molecule that condenses in the pores

(12) Gupta, R. R.; RamachandraRao, V. S.; Watkins, J. J. *Macromolecules* **2003**, *36*, 1295–1303.

(13) Dull, T. L.; Frieze, W. E.; Gidley, D. W.; Sun, J. N.; Yee, A. F. *J. Phys. Chem. B* **2001**, *105*, 4657–4662.

(14) Gidley, D. W.; Frieze, W. E.; Dull, T. L.; Sun, J.; Yee, A. F.; Yoon, D. Y. *Appl. Phys. Lett.* **2000**, *76*, 1282–1284.

(15) Mogilnikov, K. P.; Baklanov, M. R.; Shamiryan, D.; Petkov, M. P. *Jpn. J. Appl. Phys. Part 1* **2004**, *43*, 247–248.

(16) Schmidt, R.; Hansen, E. W.; Stocker, M.; Akporiaye, D.; Ellestad, O. H. *J. Am. Chem. Soc.* **1995**, *117*, 4049–4056.

(17) Lukens, W. W.; Schmidt-Winkel, P.; Zhao, D.; Feng, J.; Stucky, G. D. *Langmuir* **1999**, *15*, 5403–5409.

(18) Evans, R.; Marconi, U. M. B.; Tarazona, P. *J. Chem. Phys.* **1986**, *84*, 2376–2399.

(19) Choma, J.; Jaroniec, M.; Burakiewicz-Mortka, W.; Kloske, M. *Appl. Surf. Sci.* **2002**, *196*, 216–223.

(20) Ravikovitch, P. I.; Domhnaiill, S. C. O.; Neimark, A. V.; Schuth, F.; Unger, K. K. *Langmuir* **1995**, *11*, 4765–4772.

(21) Smarsly, B.; Goltner, C.; Antonietti, M.; Ruland, W.; Hoinkis, E. *J. Phys. Chem. B* **2001**, *105*, 831–840.

(22) Liu, J.; Zhang, X.; Han, Y.; Xiao, F.-S. *Chem. Mater.* **2002**, *14*, 2536–2540.

(23) Hedden, R. C.; Lee, H.-J.; Soles, C. L.; Bauer, B. J. *Langmuir* **2004**, *20*, 6658–6667.

(24) Hedden, R. C.; Lee, H.-J.; Bauer, B. J. *Langmuir* **2004**, *20*, 416–422.

of the film. By comparison of the refractive index (EP) or critical edge (XRP) before and after exposure to the solvent probe, volume fraction of pores that are filled by the solvent can be determined. The total film porosity is equated to the measured volume fraction of solvent in the film in the presence of saturated solvent vapor, under which conditions the condensed solvent is assumed to fill all of the pores. It is important to note that EP, XRP, PAS/PALS, and N<sub>2</sub> adsorption are all model-dependent in their determination of pore size distribution.

In this study, contrast match SANS and X-ray porosimetry are used to characterize the pore structure of a mesoporous silica film that was templated by a Pluronic\* F127 film (a block copolymer of poly(ethylene oxide) and polypropylene oxide) and synthesized in situ by impregnation from supercritical CO<sub>2</sub> solution. The pore size distribution can be evaluated from the adsorption of a probe molecule as a function of its partial pressure. Toluene was chosen as the adsorbing fluid because it generally wets the surface of these materials and previously observed adsorption properties in low-*k* films.<sup>27</sup> Additional structural and chemical characterization of the film is provided by other complementary measurements.

(\*Certain commercial equipment and materials are identified in this paper in order to specify adequately the experimental procedure. In no case does such identification imply recommendations by the National Institute of Standards and Technology nor does it imply that the material or equipment identified is necessarily the best available for this purpose.)

## Experimental Section

**Materials.** Mesoporous organosilicate films were synthesized using a supercritical carbon dioxide infusion/reaction technique.<sup>11</sup> The template was a triblock copolymer of poly(ethylene oxide)-*b*-poly(propylene oxide)-*b*-poly(ethylene oxide), PEO<sub>105</sub>-PPO<sub>70</sub>-PEO<sub>105</sub> (Pluronic F127) donated by BASF (Mount Olive, NJ) and used as received. The subscripts in the formulas refer to the average number of monomers for each segment of the copolymer. Films were spun onto approximately 50 mm<sup>2</sup> silicon wafers from an ethanol solution doped with *p*-toluenesulfonic acid (*p*-TSA) (Aldrich). The *p*-TSA is an acid catalyst for the condensation reaction. Coleman-grade carbon dioxide (CO<sub>2</sub>) was obtained from Merriam Graves and used as received. The silicate precursors, tetraethyl orthosilicate (TEOS) and methyltriethoxysilane (MTES), were obtained from Aldrich and Gelest, Inc., respectively, and used as received. Silicon wafers used in the study were kindly donated by Novellus Systems. The organosilicate precursors were then condensed within the preformed copolymer film by infusion in humidified supercritical carbon dioxide (CO<sub>2</sub>) at 60 °C and 123 bar. The reaction vessel for the 50 mm<sup>2</sup> wafers was built using two stainless steel blind hubs sealed with graphite-coated steel sealing rings. The vessel has an internal volume of approximately 160 mL and four ports for introduction and release of CO<sub>2</sub> solutions

and measurement of both temperature and pressure. The temperature of the reaction vessel was controlled using external heaters. The precursor loading ratio for the samples examined here was 2:3 for MTES:TEOS (by mass). The polymeric template was removed by calcination at 400 °C for 6 h in air. The infusion of the silicate into the film and the removal of the organic template were followed qualitatively using Fourier transform infrared spectroscopy (FTIR) (see Supporting Information).

For characterizing the microporous wall material alone, a pTSA-doped poly(ethylene oxide) (*M<sub>w</sub>* = 10 000) (Aldrich) film was spin-coated onto a similar silicon substrate. It was then exposed to a (2:3) mixture of MTES:TEOS dissolved in a humidified (near saturated) supercritical carbon dioxide (CO<sub>2</sub>) at 60 °C and 123 bar. The polymer to silicate precursor ratio was identical to the Pluronic templated film. The poly(ethylene oxide) template was then removed by calcination at 400 °C for 6 h in air.

**Thickness Characterization: X-ray Reflectivity (XR) and Spectroscopic Ellipsometry (SE).** Specular X-ray reflectivity data were collected in a  $\theta/2\theta$  geometry using Cu K $\alpha$  radiation focused by a bent crystal mirror into a 4 bounce Ge (220) crystal monochromator. The reflected beam was further collimated through a 3 bounce channel cut Ge (220) crystal before entering a proportional gas detector. Data were collected at the specular condition in all cases with the reflectivity measured as a function of the momentum transfer vector, *q*, where  $q = 4\pi/\lambda \sin(\theta)$ . From the XR data, the film thickness and electron density profile were determined from the best fit of the data using a multilayered slab routine.<sup>28</sup> To determine the film porosity, the XR was first measured under vacuum (<0.1 Pa), and then subsequently after exposure to saturated toluene vapor. The volume fraction of toluene in the film was inferred from the differential increase in bulk electron density following solvent sorption, and porosity was equated to the toluene volume fraction. All measurements were performed at ambient temperatures. The porosity was calculated from the change in the critical angle upon adsorption of toluene with the assumptions that toluene maintains its bulk liquid density when condensed in the pores and that all the pores are accessible to the solvent. For porosimetry measurements, the film was exposed to toluene vapor in air as the relative pressure of toluene (*p/p*<sub>0</sub>) was varied from 0 to 1, where *p* is the partial pressure of the toluene and *p*<sub>0</sub> is its saturated vapor pressure. In all cases, at least 30 min was allowed for the adsorbing toluene to reach equilibrium.

SE measurements were performed using GES5 spectroscopic ellipsometer (Sopra, Inc). The incident angle for all measurements was fixed at 75° from the vertical. The wavelength range examined spanned from the ultraviolet to visible range (0.25 μm to 1 μm). A four-layer model comprised of air, silicate dielectric layer of unknown thickness and refractive index, native Si oxide, and silicon crystal layer was used to fit the data. The fitting parameters were the thickness and the refractive index of the silicate dielectric layer. The refractive index of the dielectric layer was modeled using a Cauchy dispersion relationship, which has been found to be applicable for all transparent dielectric substances.<sup>29</sup>

**Chemical Characterization: Ion Beam Scattering.** The film's elemental composition was determined through a series of ion beam scattering measurements performed at the University of Pennsylvania's Laboratory for the Research on the Structure of Matter, using the NEC 5SDH Pelletron accelerator. Low-energy (1.991 MeV) forward scattering of <sup>4</sup>He<sup>+</sup> ions at shallow angles was used to establish the relative Si, O, and C ratios in the film. Forward recoil elastic scattering (FRES) with 3.418 MeV <sup>4</sup>He<sup>2+</sup> ions (using

(25) Baklanov, M. R.; Kondoh, E.; Lin, E. K.; Gidley, D. W.; Lee, H.-J.; Mogilnikov, K. P.; Sun, J. N. *Proc. Int. Interconnect Technol. Conf.* **2001**.

(26) Baklanov, M. R.; Mogilnikov, K. P. *Microelectron. Eng.* **2002**, *64*, 335–349.

(27) Lee, H.-J.; Lin, E. K.; Bauer, B. J.; Wu, W.; Hwang, B. K.; Gray, W. D. *Appl. Phys. Lett.* **2003**, *82*, 1084–1086.

(28) Ankner, J. F.; Maikrzak, C. F. *Proc. SPIE* **1992**, *1738*, 260.

(29) Gilchrist, V. A.; Lu, J. R.; Keddie, J. L.; Staples, E.; Garrett, P. *Langmuir* **2000**, *16*, 740–748.

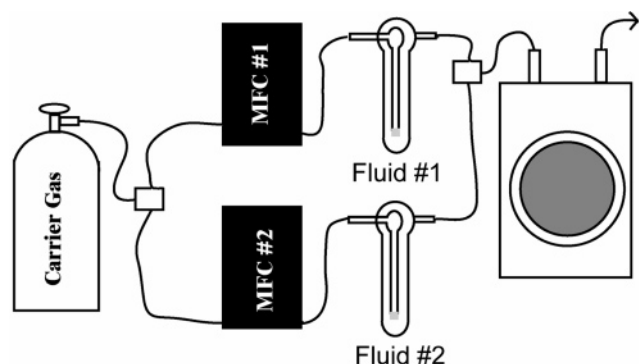


**Figure 2.** Schematic of the flow apparatus for controlling the environment. The carrier gas flow is controlled by two mass flow controllers (MFCs) and then bubbled through fluids. The streams are mixed and flow past the sample.

an aluminum stopper foil to screen out forward scattered He) was then used to measure the relative H content of the film. This relative H concentration was made absolute through calibration with a polystyrene film of known thickness and H content. Finally, resonance-enhanced grazing angle backscattering and Rutherford backscattering (RBS), also using 3.418 MeV  $^4\text{He}^{2+}$  ions, were used to fit the total film thickness in terms of the number of atoms/cm<sup>2</sup> of the film, thereby establishing the absolute Si, O, and C contents. Details of this ion beam procedure have been described previously.<sup>30</sup>

**Morphological Characterization: Small-Angle Neutron Scattering (SANS), X-ray Diffraction (XRD), and Transmission Electron Microscopy (TEM).** SANS measurements were conducted at the Center for Neutron Research at the National Institute of Standards and Technology using the 8 m NG1 instrument. The instrument configuration used for all measurements was as follows: sample to detector distance was 384 cm and neutron wavelength ( $\lambda$ ) was 6 Å with a spread ( $\Delta\lambda/\lambda$ ) of 0.12. The scattering data were corrected for sample transmission, empty cell scattering, detector sensitivity, and background scattering and scaled to absolute intensities by comparison to empty beam flux. The resultant 2-D data were circularly averaged to yield absolute scattered intensity,  $I$ , as a function of the scattering vector,  $q$ . The samples for SANS were prepared from films on silicon substrates where the sample was cut into multiple circular disks with diameter of approximately 2 cm. The SANS measurements were conducted on a film stack of 3 wafers to increase the scattered intensity. The atmosphere surrounding the stack was controlled using a custom built flow-through stainless steel scattering cell equipped with quartz windows. This assembly was placed under vacuum to minimize background scattering. The small volume in the cell surrounding the films remained at approximately atmospheric pressure during all experiments. The flow of vapor through the cell was controlled using two mass flow controllers (MKS) and confirmed by use of an exit bubbler. A schematic of the environmental control system is shown in Figure 2. The carrier gas used in these experiments was nitrogen. The total flow through the system was maintained at 10 cm<sup>3</sup> min<sup>-1</sup> during the course of all measurements. For determination of the contrast match composition, the bubblers were filled with pure d-toluene or pure h-toluene. By varying the flow rates through each individual solvent, the NSLD for the mixed stream that is passed by the mesoporous films can be controlled from either extreme. For porosimetry measurements, the same apparatus is used except that one bubbler contains a solution of contrast match solvent (d-toluene/h-toluene) and the other contains no solvent. In the same manner as the contrast was varied, the partial pressure of the contrast

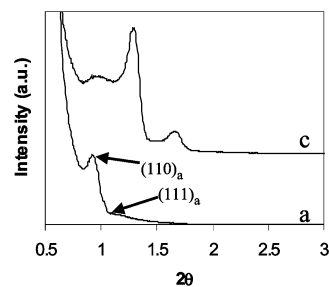


**Figure 3.** X-ray diffraction patterns for the (a) as-infused mesostructured organosilicate film and the (c) calcined mesoporous organosilicate film. The single sharp Bragg peak in the as-infused XRD pattern was assigned to the (110) reflection of a cubic mesostructure with unit cell parameter of 135 Å.

match fluid,  $p/p_0$ , can be incremented stepwise from 0 to 1. The SANS data were collected continuously in 5 min increments. The total acquisition time ranged from 60 to 150 min depending upon the intensity of the scattering observed. Equilibrium was assumed when the scattering profile remained constant. In most cases, the samples took approximately 10 min to equilibrate; however, as long as 50 min was needed to reach equilibrium for the mesopore-filling step during the porosimetry measurements.

X-ray diffraction (XRD) measurements were performed using a Philips X'Pert PW3040 diffractometer using Cu K $\alpha$  radiation ( $\lambda = 0.15418$  nm) in the conventional Bragg-Brentano  $\theta$ - $\theta$  geometry. The data were collected with  $2\theta$  varying from 0.5° to 6°, with an increment of 0.005°.

TEM was performed on the calcined mesoporous films using a JEOL 2000 FX microscope operating at 200 kV. The samples were prepared by scraping a section of film off the wafer, crushing it, and dispersing the fragments in acetone or ethanol to form a slurry. Samples for examination were prepared by evaporating drops of the slurry on Formvar resin-coated copper grids (Electron Microscopy Sciences).

## Results

**i. Film Structural Characterization: XRD, VASE, and TEM.** The XRD patterns of the as-infused (film prior to template removal) and the calcined mesoporous organosilicate films are shown in Figure 3. The XRD pattern of the as-infused film shows a single, sharp Bragg peak, corresponding to  $d$  spacing of 95.5 Å, along with a broad shoulder peak. After calcination at 400 °C in air, there is considerable shrinkage of the film normal to the substrate due to further condensation of the silicate structure and the removal of the organic template. For the calcined film, the XRD pattern shows three strong Bragg peaks corresponding to lower  $d$  spacings of 96, 68, and 53.1 Å in addition to a broad shoulder peak. The absence of multiple Bragg peaks makes an unambiguous assignment of the space group of the mesostructure present in the film difficult. However, cross-sectional SEM<sup>11</sup> and TEM suggest a cubic or distorted cubic mesostructure in the films. Distortion of the lattice would be expected from anisotropic shrinkage of the film during calcination. Figure 4 shows the TEM micrographs along the [100] and the [111] orientations of the cubic mesostructure. The combination of the XRD patterns and the electron micrographs suggests a cubic morphology for the organosilicate film. The sharp Bragg peak in the XRD pattern of the as-infused film was assigned to the (110) reflection of a 3D cubic mesostructure with a unit cell parameter of 135

(30) Bauer, B. J.; Lin, E. K.; Lee, H.-J.; Wang, H.; Wu, W. *J. Electron. Mater.* **2001**, *30*, 304–308.

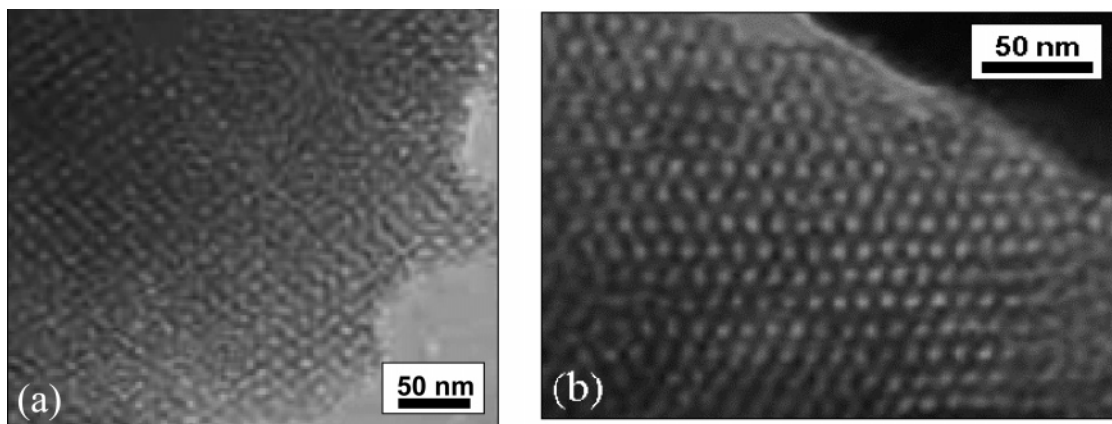


**Figure 4.** Transmission electron micrographs of the calcined mesoporous organosilicate film along the (a) [100] and (b) [111] zone axes of a cubic mesostructure. The images were acquired using a JEOL 2000 FX electron microscope operating at 200 kV.

**Table 1. Thickness and Refractive Indices of the Mesostructured Organosilicate Film**

	thickness (nm)	refractive index, $\lambda = 632$ nm
as-infused film	$1000 \pm 9.5$	1.560
calcined film	$617 \pm 4.9$	1.185

**Table 2. Elemental Composition Determined by RBS and FRES (exp) Compared to Theoretical Composition for Complete Condensation (th)**

element	%		element	%	
	exp	th		exp	th
C	8.3	6.2	O	52.2	49.2
Si	23.7	26.2	H	15.8	18.5

Å. Such an assignment is consistent with other films templated by Pluronic F127 using our approach or conventional preparations.<sup>11,31</sup> A detailed characterization is currently underway using grazing incidence small-angle X-ray scattering (GISAXS).

Spectroscopic ellipsometry (SE) measurements were performed on both the as-infused and the calcined films. The two ellipsometric angles, psi and delta, were obtained as a function of the wavelength in the range of 0.25–1  $\mu\text{m}$  at a fixed incidence of 75° and fitted using the four-layer model described previously. The thickness and the refractive indices ( $\lambda = 632$  nm) for the as-infused and the calcined films are given in Table 1. The refractive index of calcined mesoporous film,  $n_d \approx 1.19$ , lies about midway between the refractive indices of SiO<sub>2</sub> (1.45) and air (1.01), suggesting that a substantial volume fraction of porosity is present.

### ii. Chemical Characterization: Ion Beam Scattering.

The chemical composition of the calcined mesoporous film determined by ion beam scattering is reported in Table 2 and is consistent with theoretical estimates for complete condensation of the precursors. This suggests that the precursors were uniformly distributed in the film. Additionally, ion beam scattering results did not show signs of composition gradients, consistent with a uniform film composition.

### iii. Pore Characterization: SANS and XRP.

For the SANS porosimetry to be effective, the NSLD of the pore walls must be matched by the pore-filling solvent, resulting

in zero coherent scattering at the contrast match point. This means that (a) the wall material should be homogeneous such that compositional variations within the wall material do not give rise to scattering that might erroneously be interpreted as porosity and (b) that all the pores are accessible to the contrast matching solvent. The mesoporous films prepared in CO<sub>2</sub> meet these criteria, but a priori prediction of a contrast match point for this system is difficult given the multiple precursors used in the synthesis of the inorganic phase. The contrast match point was identified experimentally by exposing the sample to saturated vapors of toluene and deuterated toluene mixtures. Varying the deuterium/proton ratio in the vapor provides a means of adjusting the NSLD of the probe fluid. The scattered intensity is proportional to the square of the NSLD difference between the wall and the filled pores

$$I(q) \propto (b_w - b_t)^2 \quad (1)$$

where  $I(q)$  is the scattered intensity,  $q$  is the scattering vector, and  $b_i$  is the NSLD for the wall (w) and toluene mixture (t), respectively. Figure 5 shows the corrected 2-D data from several of the different compositions. For the composition extremes of fully protonated or deuterated toluene, the scattering exhibits a strong maximum at finite  $q$ , corresponding to the primary Bragg spacing. As the composition is varied from these extremes, the intensity of the Bragg peak decreases, indicative of weaker contrast between the adsorbed solvent and the wall material. At a composition of 40% d-toluene and 60% h-toluene by volume, the Bragg peak disappears completely and only spill over from the beam stop remains in the scattering. This composition is close to the contrast match point. By definition the contrast match point should correspond to the condition where  $I(q) = 0$  (i.e., when  $b_w = b_t$  in eq 1). However, the minimum in the scattering does not coincide with  $I(q) = 0$  because of residual incoherent scattering ( $q$  independent flat background) as illustrated in Figure 6. Nevertheless, the minimum still defines the contrast match point and corresponds to a composition of 41% d-toluene or a NSLD of  $2.88 \times 10^{-6}$  Å<sup>2</sup>. The NSLD is calculated based on the assumption that the adsorbed toluene in the pores has the same density as the bulk toluene liquid. From the contrast match point and the chemical composition of the film from the ion beam

(31) Soler-Illia, G. J. A. A.; Crepaldi, E. L.; Grosso, D.; Durand, D.; Sanchez, C. *Chem. Commun.* **2002**, 20, 2298–2299.

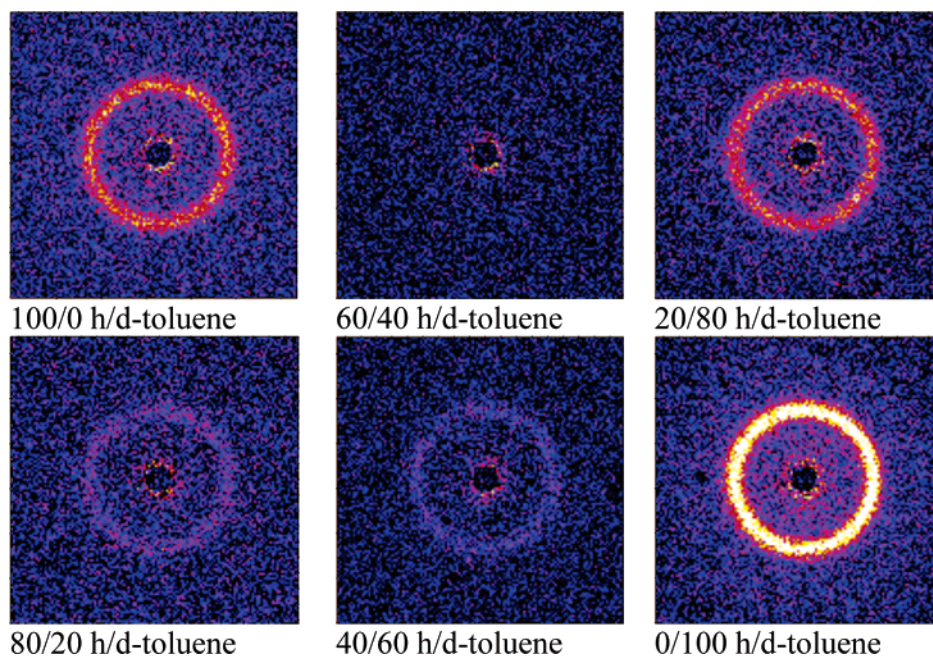


**Figure 5.** Qualitative determination of contrast match point using saturated toluene vapor with differing d/h ratios. The 2-D images clearly show the decay and reemergence of the Bragg peak as the % d-toluene is increased from 0% to 100%. The peak appears to completely vanish when exposed to saturated toluene vapor containing 40% d-toluene. The scale on the images are all from  $I = (0 \text{ to } 22) \text{ cm}^{-1}$ .

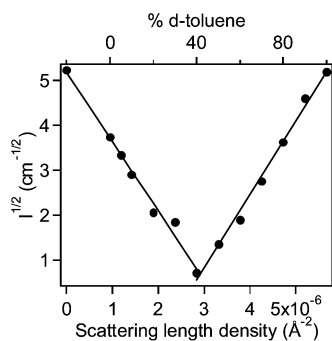


**Figure 6.** Quantitative determination of the contrast match point using saturated toluene vapor with differing d/h ratios. The square root of the intensity at the Bragg peak position ( $q^*$ ) is shown as a function of both neutron scattering length density and %d. The negative %d corresponds to the sample in air. The contrast match point is at  $2.88 \times 10^{-6} \text{ Å}^{-2}$ .

scattering data (Table 2), the pore wall mass density can be determined. The scattering length density is the weighted average of the atomic composition on a molar basis multiplied by the mass density. The mass density of the wall material ( $\rho_m$ ) is then calculated as

$$\rho_m = \frac{\text{NSLD}_{\text{match}}}{N_A \sum b_i x_i} \sum m_i x_i \quad (2)$$

where  $\text{NSLD}_{\text{match}}$  is the scattering length density at the match point ( $2.88 \times 10^{-6} \text{ Å}^{-2}$ ),  $N_A$  is Avogadro's number,  $b_i$  is the scattering length of the  $i$ th element in the wall material,  $x_i$  is the mole fraction of the  $i$ th element for the dry wall material as determined by ion beam analysis, and  $m_i$  is the mass density. The calculated density ( $\rho_m$ ) is  $1.95 \text{ g cm}^{-3}$ , which is a reasonable value for a condensed silicate.

Returning to the SANS profile for the mesoporous material without solvent, the scattering shows several distinct features as illustrated in Figure 7. (The data throughout the manuscript

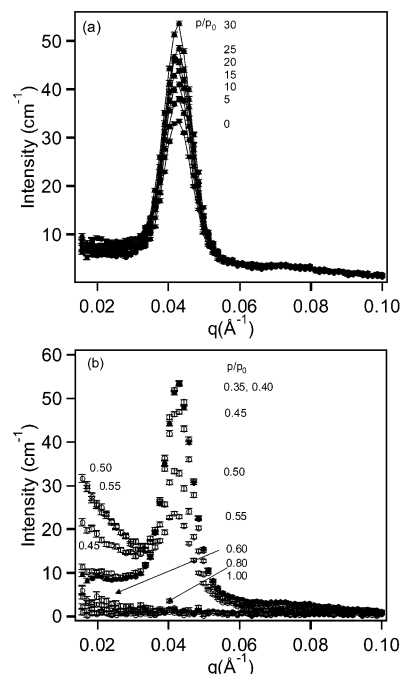


**Figure 7.** SANS porosimetry data for mesoporous silicate film. The partial pressure of the contrast match d-h-toluene mixture is increased from zero to saturation and the changes in the scattering profiles can be related to the pore-filling process. (a) The initial pore filling results in an increase in the contrast of the mesopores by filling micropores in the wall material. (b) Further increase in the partial pressure of the contrast match fluid results in filling of the mesopores. By  $p/p_0 = 0.60$ , almost all the pores are filled.

and the figures are presented along with the standard uncertainty ( $\pm$ ) involved in the measurement based on one standard deviation.) A primary Bragg reflection at  $q = 0.0425 \text{ Å}^{-1}$  ( $d$  spacing  $\approx 148 \text{ Å}$ ) dominates the scattering; a weaker reflection at  $q = 0.0728 \text{ Å}^{-1}$  ( $d$  spacing  $\approx 86 \text{ Å}$ ) is also visible, albeit less pronounced. In addition, there is a monotonically decreasing intensity component on which the

Bragg reflections lie. This component can be fit with the Debye-Anderson-Brumberger (DAB) function:<sup>32</sup>

$$I(q) = \frac{8\pi\phi_0(1 - \phi_0)\rho_m^2\sigma_m^2\xi^3}{(1 + \xi^2q^2)^2} \quad (3)$$

where  $\phi_0$  is the volume fraction of one phase,  $\rho_m$  is the mass density of the wall,  $\sigma_m$  is the total neutron scattering length per unit mass, and  $\xi$  is the correlation length. This correlation length for the DAB fit is approximately  $\xi \approx 11$  Å for the sample in air. The source of these characteristic length scales will be discussed later.

It has been shown that the wall density can be determined through a contrast match SANS experiment. The pore size distribution (PSD) can also be determined using the contrast-matched SANS technique by varying the partial pressure of the contrast match solution in a manner similar to BET measurements. With the BET or other conventional porosimetry techniques, the pore size distribution is obtained indirectly by monitoring the amount of adsorbed condensate and invoking a geometric model of adsorption to convert the mass or volume of condensate to a size. However, with SANS, the characteristic length scale of the porosity (whether it is  $\xi$  for DAB type scattering or the spacing of a Bragg diffraction peak) can be determined directly by fitting the scattering data. The  $q$ -dependent characteristics of the scattering data provide valuable insight into the pore geometry. So while contrast-matched SANS and traditional forms of porosimetry are both model-dependent in their interpretations, SANS porosimetry provides a self-consistency check of the validity of the model.

Figure 7 shows the SANS porosimetry profiles during the filling process for the mesoporous film. At low partial pressures, there is little change to the general shape of the scattering profiles. The DAB scattering remains constant at high  $q$ , but the intensity of the primary Bragg reflection increases with increasing partial pressure up to  $p/p_0 = 0.35$ . There is a small increase in scattering at low  $q$ , which would be consistent with an increase in the contrast between the templated mesopores and the wall material due to filling of the micropores in the wall material. There is also very little change in the DAB scattering below  $p/p_0 = 0.35$ . This indicates that the DAB type scattering does not reflect the micropores in the wall material itself. Hence, the micropores in the wall material must be smaller than the resolution of the instrument (i.e., correlations smaller than several Å). A similar scenario was observed in SANS measurements on chemical vapor deposited low- $k$  dielectric films.<sup>33</sup> The pores were too small to be observed in SANS measurements, but the density of the film could still be increased appreciably by infiltrating the micropores with toluene. There is no change in the scattering profile as  $p/p_0$  is increased from 0.35 to 0.40. This indicates that the micropores are completely filled once  $p/p_0$  reaches 0.35.

When  $p/p_0$  is greater than 0.40, the Bragg peak intensity begins to decrease, indicative of mesopore filling as shown

**Table 3. Primary Peak Position ( $q^*$ ) as a Function of  $p/p_0$**

$p/p_0$	$q^*$ (Å <sup>-1</sup> )	$\Delta q^*$ (Å <sup>-1</sup> )	$I(q^*)$ (cm <sup>-1</sup> )
0	0.0425	0.0000	34.7
5	0.0425	0.0000	39.1
10	0.0425	0.0000	42.3
15	0.0425	0.0000	44.3
20	0.0425	0.0000	47.6
25	0.0425	0.0000	49.7
35	0.0425	0.0000	54.3
40	0.0424	0.0001	54.9
45	0.0417	0.0008	44.7
50	0.0413	0.0012	32.1
55	0.0407	0.0018	23.8

**Table 4. Fit Parameters for the Low  $q$  Scattering from the Partial Filling of Mesopores and Comparison to Filling Determined by Bragg Peak Intensity**

$p/p_0$	$\xi$ (Å)	$\phi$ (fit)	$\phi$ (Bragg)
0.45	31.3	0.15	0.18
0.50	39.1	0.48	0.42
0.55	44.3	0.63	0.57

in Figure 7b. Interestingly, the DAB scattering at high  $q$  also begins to decrease at the same time as the scattering from the mesopores. Thus, the source of the DAB scattering is coupled to the mesopore filling. There is an additional feature that appears in the scattering as the pores fill at low  $q$ , where the scattering actually increases. Notice that there is also a slight polydispersity to the pore size distribution, indicated by the shift in the primary Bragg diffraction peak position as the mesopores fill as shown in Table 3; this polydispersity could lead to the low  $q$  scattering changes as the mesopores progressively fill.<sup>21</sup> The peak positions are determined by a Lorentzian fit of the data in the range of the primary peak. The position of the Bragg diffraction peaks reflect the distance between pores and is not a direct measure of the pore radius. The scattering at low  $q$  is related to both the fraction of the mesopores that are filled ( $\phi$ ) and the distance between the unfilled regions ( $\xi$ ). The low  $q$  upturn can be modeled as

$$I(q) = \phi(1 - \phi)\Delta b^2 \frac{1}{(1 + \xi^2q^2)} \quad (4)$$

where  $\Delta b^2$  is the contrast factor between the unfilled pore and the wall/filled pore regions. Note that the wall and the filled pores have identical NSLD. The fraction of filled mesopores as determined by the fit with eq 4 can be checked against the Bragg peak intensity, as this intensity is also proportional to the number of scattering objects (i.e., volume fractions). From the Bragg peak intensity, the fraction of filled mesopores as a function of partial pressure ( $0.40 < p/p_0 < 0.55$ ) can be calculated as

$$I(q^*)_{p/p_0} = (1 - \phi)I(q^*)_{p/p_0=0.4} \quad (5)$$

Table 4 shows the results from the fits as well as a comparison of the fraction of filled mesopores from the fit and the measured Bragg intensity. The agreement between the two methods is reasonably good and the appearance of the low  $q$  scattering can be attributed to the partial filling of the mesopores. The correlation length ( $\xi$ ) also increases as the partial pressure increases and the smaller mesopores are filled, as would be expected. Once  $p/p_0$  reaches 0.60, almost

(32) Debye, P.; Anderson, R.; Brumberger, H. *J. Appl. Phys.* **1957**, *28*, 679.

(33) Lee, H.-J.; Soles, C. L.; Liu, D.-W.; Bauer, B. J.; Lin, E. K.; Wu, W.; Grill, A. *J. Appl. Phys.* **2004**, *95*, 2355.

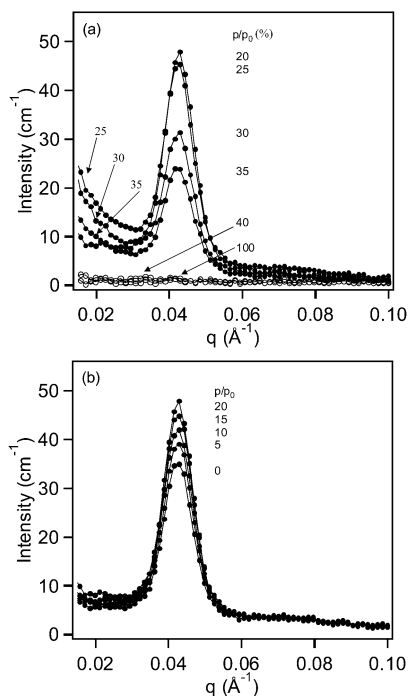


**Figure 8.** SANS porosimetry data for mesoporous silicate film. The partial pressure of contrast match fluid is decreased from saturated and the pore-emptying process is examined. (a) Once the pores are filled, no emptying occurs until the partial pressure is reduced to less than 0.40. (b) The intensity of the Bragg peak decreases as the partial pressure is decreased from 0.20 to 0.

all the pores are filled as evidenced by the lack of the Bragg peak, but some pores remain and contribute to a small amount of low  $q$  scattering. At  $p/p_0 = 0.80$ , all of the pores are filled and the scattering profile is featureless, corresponding to the incoherent background scattering of the sample. The pore polydispersity is responsible for the observed DAB contribution to the scattering.

After the film is exposed to saturated vapor, the partial pressure is decreased stepwise to examine the pore-emptying process, with the corresponding scattering profiles shown in Figure 8. As expected for mesoporous materials, the porosimetry loop shows hysteresis. The mesopores do not begin to drain until  $p/p_0$  is decreased to 0.35. At this point, the Bragg scattering from the ordered nature of the mesopores re-appears. The intensity of the Bragg peak increases as  $p/p_0$  is further decreased, indicating the emptying of additional mesopores. As with pore filling, the DAB scattering re-appears with the Bragg scattering. When the pores begin to empty, there is significant scattering at low  $q$  as was observed when the mesopores were filling, due to the polydispersity of the pores. As the partial pressure of the contrast match fluid is further decreased, the intensity of the Bragg peak continues to grow, but the low  $q$  scattering diminishes. However, once  $p/p_0$  reaches 0.20, the scattering intensity of the Bragg peak begins to decrease with decreasing partial pressure. This decrease is due to the small micropores in the wall matrix emptying, thus decreasing the contrast between the walls and mesopores. Again, these micropores are not observed directly in the scattering data because their size is smaller than can be resolved with SANS. The microporosity of the wall material can be calculated from the intensity change of the Bragg peak. The scattering

intensity is proportional to the square of the contrast (eq 1). Thus, the porosity of the wall material is

$$P_{\text{micropores}} = 1 - \sqrt{\frac{I_{\text{air}}}{I_{\text{max}}}} \quad (6)$$

where  $I_{\text{max}}$  is the maximum intensity of the Bragg peak upon filling ( $p/p_0 = 0.35$ ). Equation 6 yields a microporosity of 0.21. Typical microporosity of mesoporous materials prepared from solution-based synthesis routes ranges from 0.04 to 0.10,<sup>7,8,21,34</sup> although greater degrees of microporosity have been observed for materials prepared at high TEOS:surfactant molar ratios.<sup>35,36</sup> The maximum intensity on pore emptying is not as large, presumably due to the mesopores never being fully empty and all the micropores filled. This transition is expected to be rather sharp and given the coarseness of the partial pressure steps it is not surprising that the maximum intensities do not agree. The consistency between the adsorption and desorption legs in the micropore filling will be shown later.

To complement information from SANS porosimetry, specular X-ray reflectivity porosimetry (XRP) was also performed. Both techniques are based on gradually increasing or decreasing the partial pressure of an organic vapor (toluene in this case) surrounding the sample. As previously described, SANS allows for morphological characterization of the pore structure during pore filling if a contrast-matched condensate is employed. From the X-ray measurements, the morphology is not directly characterized. Rather, the average film density is monitored as toluene either condenses or evaporates from the porous film. This pore-filling/-draining is manifested as a significant shift (increase/decrease) in the critical edge ( $Q_c$ ) for total external X-ray reflectance of the mesoporous film (in this case, it is not particularly important that the electron density of the film did not contrast match with the electron density of the toluene). The wall mass density ( $\rho_w$ ) and porosity ( $P$ ) of the film can be determined using the rule of mixtures, knowing the critical edge of the film under vacuum and when exposed to saturated toluene vapor, and knowing the film composition as determined by the ion beam scattering by solving the following equations:

$$\rho_{\text{ave}} = \rho_w(1 - P) \quad (7)$$

$$\rho_{\text{ave,toluene}} = \rho_w(1 - P) + \rho_{\text{toluene}}P \quad (8)$$

where  $\rho_{\text{ave}}$ ,  $\rho_w$ ,  $\rho_{\text{ave,toluene}}$ , and  $\rho_{\text{toluene}}$  are the average density of the mesoporous film, density of the wall material, average density of the mesoporous film when exposed to saturated toluene vapor, and density of toluene condensed in the pores (0.865 g cm<sup>-3</sup>), respectively.

From the X-ray reflectivity measurements, the wall density was determined to be 1.92 g cm<sup>-3</sup> with a total film porosity of 0.39 by volume. This value of porosity includes the

(34) Smarsly, B.; Xomeritakis, G.; Yu, K.; Liu, N.; Fan, H.; Assink, R. A.; Drewien, C. A.; Ruland, W.; Brinker, C. J. *Langmuir* **2003**, *19*, 7295–7301.

(35) Kruk, M.; Jaroniec, M.; Joo, S. H.; Ryoo, R. *J. Phys. Chem. B* **2003**, *107*, 2205–2213.

(36) Van Der Voort, P.; Benjelloun, M.; Vansant, E. F. *J. Phys. Chem. B* **2002**, *106*, 9027–9032.

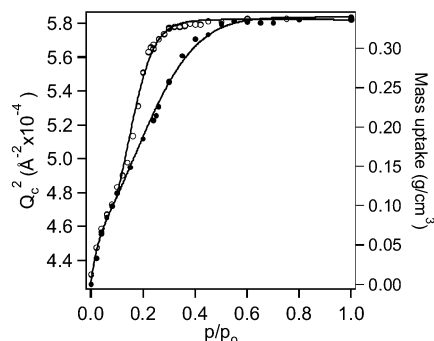


**Figure 9.** X-ray porosimetry characterization of the mesoporous film. The pore-filling (●) and -emptying (○) cycles are shown. The change in the critical edge ( $Q_c$ ) is directly related to the amount of toluene condensed in the pores as shown on the right axis. The solid lines are fits of the data to a Sigmoidal and Gaussian series.

mesopores and the micropores because the X-ray technique does not distinguish how solvent molecules are partitioned on the length scale of the pores. The measured wall density is in good agreement with the density determined from the SANS contrast match ( $1.95 \text{ g cm}^{-3}$ ). By tracking the change in the critical edge with partial pressure of toluene, the fraction of pores filled at each condition can be determined as shown in Figure 9. The filling and emptying behavior of the mesoporous film is similar to those observed for block copolymer templated silicates using sol-gel chemistry.<sup>17</sup> As probe solvent  $p/p_0$  is increased, there is initially a steep adsorption process due to the presence of micropores at low  $p/p_0$ , followed by adsorption in the mesopores at higher  $p/p_0$ . There is also a hysteresis loop between the filling and emptying of the mesopores. From the change in  $Q_c^2$ , the mass of toluene adsorbed at each condition can be determined as

$$m_{\text{toluene}} = \frac{(\rho_e - \rho_{e,\text{vac}})MW_{\text{toluene}}}{n_{e,\text{toluene}}N_A} \quad (9)$$

with

$$\rho_e = \frac{2\pi\delta x}{Q_c^2 r_0} \text{ and } \delta x = \frac{\theta_c^2}{2} = \frac{\left(\arcsin\left[\frac{\lambda\sqrt{Q_c^2}}{4\pi}\right]\right)^2}{2}$$

where  $\rho_e$  is the electron density of the film,  $MW_{\text{toluene}}$  is the molecular weight of toluene,  $n_{e,\text{toluene}}$  is the total number of electrons in toluene atom (50),  $N_A$  is Avogadro's number,  $r_0$  is the radius of an electron ( $2.82 \times 10^{-5} \text{ \AA}$ ), and  $\lambda$  is the X-ray wavelength ( $1.54 \text{ \AA}$ ). The mass uptake is shown on the right axis of Figure 9.

Transformation of the adsorption/desorption isotherms into a PSD for mesoporous materials (2–50 nm pores) requires a model that accounts for capillary condensation. The Kelvin equation offers the simplest relation between  $P/P_0$  and pore size:<sup>38</sup>

$$r_c = \frac{2V_m\gamma}{-RT} \frac{1}{\ln(P/P_0)} \quad (10)$$

where  $r_c$  is the critical radius for capillary condensation at the partial pressure,  $P$ , and  $P_0$  is the equilibrium vapor pressure,  $\gamma$  is the liquid surface tension, and  $V_m$  is the molar

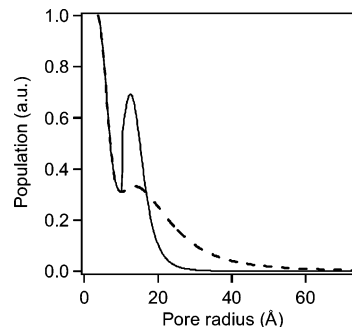


**Figure 10.** Pore size distribution for fits of the toluene mass uptake obtained from the change in the critical edge of the film (Figure 11). The PSD is calculated for pore filling (dashed line) and pore emptying (solid line).

volume. Although the Kelvin equation is not expected to yield accurate pore size estimation, it does provide a qualitative description of the PSD.<sup>39</sup>

The data in Figure 9 were fit to the sum of sigmoidal and Gaussian series to better estimate the PSD. The fit is arbitrary in that it is only important that the curve fit accurately parametrize the  $p/p_0$  dependence of the physisorption isotherms. Regardless of the analytical fit function employed, the PSD is estimated by using the Kelvin equation to transform the fit function into the PSD that is shown in Figure 10. The PSD contains many very small pores as expected from the SANS data and a peak from the mesopores at a pore radius of  $12.8 \text{ \AA}$  is observed using the data from the desorption leg of the isotherm (assuming the Kelvin equation describes the isotherm). It should be noted that this PSD is in terms of the relative population and not corrected for the total or absolute volume of pores.

The estimate of the average pore radius from the Kelvin equation can be compared to the pore radius determined from the SANS Bragg peak position. Recall that the Bragg diffraction peak corresponds to the distance between mesopore centers ( $l$ ):

$$l = \frac{2\pi}{q^*} \quad (11)$$

where  $q^*$  is the primary Bragg peak location. Assuming a primitive cubic array of spherical pores, the radius of the pores ( $r$ ) is related to the cubic unit cell parameter ( $a$ )

$$r = \left(\frac{3}{4\pi}\right)^{1/3} P^{1/3} a \quad (12)$$

where  $P$  is the mesopore fraction. Based upon the microporosity calculated from SANS (0.21) and the total film porosity (0.39), the mesoporosity of the film is 0.18. From

(37) Liu, T.; Wan, Q.; Xie, Y.; Burger, C.; Liu, L.-Z.; Chu, B. *J. Am. Chem. Soc.* **2001** *123*, 10966–10972.

(38) Barrett, E. P.; Joyner, L. G.; Halenda, P. H. *J. Am. Chem. Soc.* **1951**, *73*, 373. Broekhoff, J. C. P.; de Boer, J. *Catalysis* **1967**, *9*, 8.

(39) More complex models, which are based on corrections to the Kelvin equation, have been developed to describe the pore filling of mesoporous materials.<sup>38</sup> Even with these additional parameters, quantitative estimates of the PSD can be more than 100% in error for pores less than 20 nm, and none of the existing interpretations of capillary condensation yield reliable pore sizes.<sup>40</sup> More accurate interpretations require computer modeling and/or simulations of the isotherms such as Gage Cell Monte Carlo (GCMC) simulations or nonlinear density functional theory (NLDFE) methods. Given these constraints, the Kelvin equation in its simplest form has been used to provide a qualitative estimate of the PSD for this material.

the XRD measurement (Figure 3), the (100) plane spacing of the as-infused sample (135 Å) corresponds well to the 148 Å spacing obtained from the SANS measurements on the calcined film. The presence of (100) reflection for a primitive cubic mesostructure has been previously observed for some Pluronic templated mesostructures.<sup>37</sup> The absence of the shift of the Bragg reflection to lower  $d$  spacing in the SANS data upon calcination is consistent with anisotropic film shrinkage. The XRD measurement, for which the shift is observed, is sensitive to the through plane spacing, whereas SANS probes in-plane correlations. The XRD data ( $a = 135$  Å) and eq 12 yield an estimate of the pore radius of 47 Å, which is slightly greater than the pore radius obtained from the TEM micrographs (25–30 Å). As expected,<sup>40</sup> the Kelvin equation underestimates the pore radius significantly (12.8 Å).

The physisorption isotherms in Figure 9 can also be used to estimate the level of microporosity by assuming that mesopore filling only occurs in the hysteresis loop. By this definition the micropores account for approximately 44% of the total film porosity, i.e., a microporosity of 0.17. The microporosity calculated from the XRP measurements (0.17) agrees well with the SANS data (0.21). Additionally, the X-ray and SANS porosimetry physisorption isotherms are in qualitative agreement. From the X-ray measurements, the pores are not completely filled until  $p/p_0 = 0.60$ , which is identical to the partial pressure where the Bragg scattering disappears in the SANS data upon filling. Similarly from the X-ray measurements, the initial emptying of the pores begins at a partial pressure of ca. 0.30, while from the SANS data emptying of the mesopores begins at 0.35. The increase in scattering at low  $p/p_0$  from the SANS, which has been attributed to small micropores, is also consistent with the pronounced toluene absorption into the micropores at low  $p/p_0$  in the X-ray porosimetry.

To explore the origins of the microporosity, SANS porosimetry was performed on a film comprised solely of wall material without mesopores. The film is synthesized by infusing and reacting the organosilicate precursors within a poly(ethylene oxide) (PEO) homopolymer film. In this way, micropores are formed (templated) by the removal of the PEO during calcinations. One of the difficulties with this measurement was the low inherent scattering in the sample. Since many scattering experiments were necessary for the porosimetry, the statistics were limited by the available beamtime. However, as can be seen in Figure 11a, the difference between the unfilled and pores filled with the contrast-matched toluene fluid (same composition as for the mesoporous film) is evident and greater than the standard uncertainty in the data. These materials (Pluronic-templated and PEO-templated) appear similar in all regards except for the presence of mesopores. The nonmesoporous film also exhibits DAB scattering with a  $\xi$  of approximately 11 Å in the unfilled state, similar to the mesoporous material. However, we are not sure of this significance of these similar

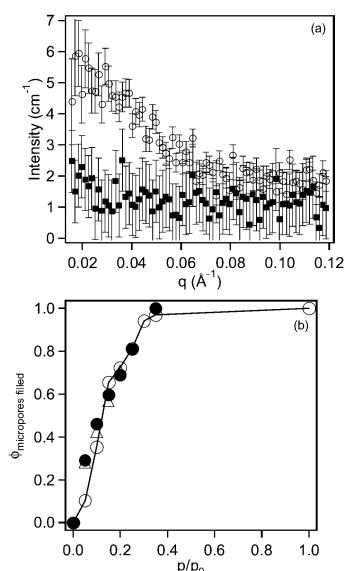


**Figure 11.** SANS porosimetry on PEO-templated silicate. (a) The scattering of the film is weak in comparison to the mesoporous sample, but the difference in scattering in air (○) and when exposed to saturated contrast match vapor (same composition as Figures 7 and 8) (●) is observable. (b) The filling of the micropores in the PEO-templated silicate (○) can be followed using the change in the maximum scattering intensity with partial pressure of contrast match fluid. The filling (●) and emptying (△) of the micropores in the mesoporous material matches the micropore filling of the PEO-templated material.

correlations length. The similarity may be coincidental as described below.

Due to the poor statistics in Figure 11a, it is difficult to accurately extract information about the size of  $\xi$  as a function of partial pressure. However, the changes in the scattering intensity with partial pressure are easy to resolve. The change in the intensity is related to the volume fraction of micropores filled ( $\phi_{\text{micropores filled}}$ ) as

$$\phi_{\text{micropores filled}} = 1 - \frac{I_{q=0} - I_{\text{CM}}}{I_{\text{Air}} - I_{\text{CM}}} \quad (13)$$

where  $I_{q=0}$  is the extrapolated scattering intensity at  $q = 0$  at partial pressure of interest,  $I_{\text{CM}}$  is the baseline intensity at  $p/p_0 = 1.0$ , and  $I_{\text{Air}}$  is the extrapolated scattering intensity in air ( $q = 0$ ). The scattering decreases rapidly as the micropores are filled, and complete filling appears to occur by  $p/p_0 = 0.35$ . In contrast for the mesoporous film from the SANS profiles in Figure 7, the scattering at high  $q$  that contains the DAB scattering does not decrease until the scattering intensity of the Bragg peak also decreases; there is no decrease in the DAB scattering in the mesoporous material until  $p/p_0 > 0.35$ . This is a significant difference in the pore-filling and -emptying characteristics of the DAB scattering between the Pluronic- and PEO-templated films, despite the similar  $\xi$ 's. It appears that the source of the DAB scattering is different in the two materials. However, the micropore filling of the two materials can be compared by examining the Bragg peak intensity in the mesoporous material at each  $p/p_0$  during the pore-filling (and pore-emptying) process.

$$P_{\text{micropores}} = 1 - \sqrt{\frac{I_{\text{air}}}{I_{p/p_0}}} \quad (14)$$

(40) Neimark, A.; Ravikovitch, P. I.; Vishnyakov, A. *Phys. Rev. E* **2000**, *62*, R1493. Neimark, A. V.; Schuth, F.; Unger, K. K. *Langmuir* **1995**, *11*, 4765. Ravikovitch, P. I.; Vishnyakov, A.; Neimark, A. *Phys. Rev. E* **2001**, *64*, 011602.

A comparison of the micropore filling between the two films is shown in Figure 11b. The micropore filling in the two materials is nearly identical. Thus, the source of the micropores in the mesoporous sample is due to the templating of the PEO segments in the mesopore wall. Additionally, the micropore filling and emptying in the mesoporous material is consistent with the XRP data that shows no hysteresis in the micropores.

### Conclusions

Contrast variation SANS and X-ray porosimetry provide detailed structural information for mesoporous silicates. Two distinct populations of pores are present in films prepared by phase-selective deposition of organosilicate precursors in pre-organized block copolymer templates diluted with supercritical carbon dioxide. Mesopores are produced by the removal of the hydrophobic domain of the template, while micropores are produced by removal of the hydrophilic component from the silicate network that comprises the wall material. The micropores comprise a significant fraction of

the total porosity (approximately 50%) in the films. High porosity in films with spherical mesopore structures may be particularly important for the fabrication of ultralow dielectric constant films.

**Acknowledgment.** B.D.V. and R.C.H. acknowledge support of the NIST/NRC postdoctoral fellowship program. J.J.W. acknowledges financial support from NSF (CTS- 0304159). Facilities supported by the NSF Materials Research Science and Engineering Center at University of Massachusetts were used in this work. We acknowledge the support of the National Institute of Standards and Technology, U.S. Department of Commerce, in providing the neutron research facilities used in this work. The authors would like to thank Derek Ho and Charles Glinka for their assistance with the SANS measurements.

**Supporting Information Available:** Additional experimental details, figure, and table (PDF). This material is available free of charge via the Internet at <http://pubs.acs.org>.

CM048654K